Commodity WiFi Can Capture Your Respiration Even the Motion Interference Exists

MENG WANG, Hefei University of Technology, China
JINYANG HUANG*, Hefei University of Technology, China
XIANG ZHANG, University of Science and Technology of China, China
ZHI LIU, The University of Electro-Communications, Japan
MENG LI, Hefei University of Technology, China
PENG ZHAO, Hefei University of Technology, China
XINYU LI, Hefei University of Technology, China
YUANHAO FENG, The University of Electro-Communications, Japan
FUSANG ZHANG, Beihang University, Institute of Software, Chinese Academy of Sciences and Inspur Computer Technology Co., Ltd, China

As one widely used wireless technique, WiFi has the potential to perform non-contact monitoring of respiration. While pioneering works have demonstrated promising performance, they inevitably ignore the impact of pervasive motion interference caused by non-target body areas or nearby surrounding interferers. Furthermore, motion interference has a significant negative impact on the accuracy of respiration monitoring due to signal aliasing, which further decays the recognition accuracy of these systems. To tackle these limitations, by employing a novel beamforming algorithm, we propose *Wi-Spatial*, an anti-motion interference respiration monitoring system based on commodity WiFi devices that can robustly mitigate the motion interference of non-target persons and further effectively extract the respiration signals from the target person. *Wi-Spatial* first enables stable beam pattern generation of channel state information (CSI) via adaptive phase shift compensation. Then, a directional nulling beamforming (DN-BF) scheme that directs the main lobe toward the target subject while adaptively placing beam nulls in the directions corresponding to the interferer is proposed to enhance the signal response in the area where the target subject is located. Extensive experiments have demonstrated that *Wi-Spatial* achieves high performance in monitoring respiration under various intensity motion inferences, especially in high-intensity motion interference, with a median absolute deviation of 0.41 bpm, which outperforms the state-of-the-art solutions by 28%.

CCS Concepts: • **Human-centered computing → Ubiquitous and mobile computing systems and tools**.

*Corresponding author. E-mails: hjy@hfut.edu.cn

Authors' addresses: Meng Wang, mengw512@mail.hfut.edu.cn, Hefei University of Technology, Hefei, Anhui, China, 230601; Jinyang Huang, hjy@hfut.edu.cn, Hefei University of Technology, Hefei, Anhui, China, 230601; Xiang Zhang, zhangxiang@ieee.org, University of Science and Technology of China, Hefei, Anhui, China, 230026; Zhi Liu, liuzhi@uec.ac.jp, The University of Electro-Communications, Tokyo, Japan; Meng Li, mengli@hfut.edu.cn, Hefei University of Technology, Hefei, Anhui, China, 230601; Peng Zhao, ZhaoPengWork@mail.hfut.edu.cn, Hefei University of Technology, Hefei, Anhui, China, 230601; Xinyu Li, 2021111086@mail.hfut.edu.cn, Hefei University of Technology, Hefei, Anhui, China, 230601; Yuanhao Feng, fyhace@mail.ustc.edu.cn, The University of Electro-Communications, Tokyo, Japan; Fusang Zhang, fusang@iscas.ac.cn, Beihang University, Institute of Software, Chinese Academy of Sciences and Inspur Computer Technology Co., Ltd, Beijing, China.

ACM 0004-5411/2025/8-ART111
https://doi.org/XXXXXXX.XXXXXXX

Additional Key Words and Phrases: WiFi sensing, motion interference, respiration monitoring, and Channel State Information (CSI) beamforming.

ACM Reference Format:
Meng Wang, Jinyang Huang, Xiang Zhang, Zhi Liu, Meng Li, Peng Zhao, Xinyu Li, Yuanhao Feng, and Fusang Zhang. 2025. Commodity WiFi Can Capture Your Respiration Even the Motion Interference Exists. *J. ACM* 37, 4, Article 111 (August 2025), 25 pages. https://doi.org/XXXXXXX.XXXXXXX

1 INTRODUCTION

Respiration information is one of the main factors reflecting human health status. It could indicate physical and mental health conditions of a human person[29, 46], and has enabled a wide range of healthcare applications, such as sleep status monitoring[12, 44], fatigue detection[33, 37], and post-illness recovery status monitoring[36, 45]. Traditional approaches for respiration monitoring depend on wearable sensors such as pulse and capnometers[17], which need to be attached to human bodies and may further make subjects uncomfortable. Apparently, these approaches are intrusive and inconvenient to use, especially for elderly people. In the past few years, both academia and industry have devoted efforts to developing contact-free respiration monitoring systems to address the limitations of wearable and intrusive sensors. Basically, the contact-free approaches leverage the reflected signal of various media (*e.g.*, light, acoustic, WiFi, Bluetooth, other radar signals, *etc.*) to detect the subtle human chest movements of breathing [3, 9, 10, 30, 36, 41, 47]. Among all of them, WiFi [36, 41, 47], has emerged as a promising option due to its low cost, widespread deployment of indoor environments, and the capability to repurpose pre-existing communication infrastructure. Moreover, it is less susceptible to Line-of-Sight (LoS) occlusion, which seriously affects light/vision-based and short-wavelength Radio Frequency (RF)-based solutions.

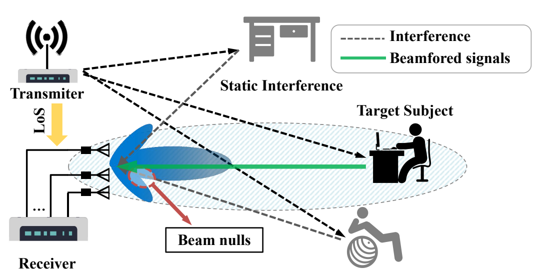

Fig. 1. Overview. *Wi-Spatial* performs CSI-based Directional Nulling BeamForming (DN-BF) algorithm to strengthen the signal from the direction of the target subject (with the main lobe) while suppressing the interference from interference directions (with the beam nulls).

Q1: What requirements should a practical wireless respiration monitoring system meet?

Although showing promising progress, existing WiFi-based respiration monitoring systems are still far from practical due to their susceptibility to motion interference from non-target body areas or individuals. The main reason is that the WiFi channel state information (CSI) tends to capture all motion information within the sensing area, which inevitably leads to potential indistinctness [22]. Existing approaches assume a stationary sensing environment and primally rely on spectral analysis of the CSI amplitude or phase to obtain the respiration rate over a period of time [13, 44]. However, such a strong assumption of a stationary environment is unrealistic, as dynamic motion interference is pervasive in practical environments. Furthermore, in such situations, the respiratory signals reflected from the target person are entangled with the motion noise from non-target individuals, which can potentially lead to overestimation of the target's respiration information. Thus, these systems inevitably fail to work properly when non-target individuals are present. Obviously, an anti-motion interference WiFi-based respiration monitoring system that can extract respiration signals under pervasive human motion interference scenarios is necessary and valuable.

To address the motion interference issue, a straightforward way is to filter out the motion signal of non-target persons while preserving the respiration of the target person (*i.e.*, spatial filtering, also known as beamforming). The basic idea of beamforming is to strengthen the signal from a specific direction. Hence, signals from other directions are much weaker and thus do not interfere with the sensing at the specific direction. Therefore, we ask the question,

> **Q2:** Can we achieve anti-motion interference sensing in the area-of-interest via CSI beamforming with one pair of commodity WiFi transceivers?

Although the idea of CSI beamforming-based anti-motion interference sensing sounds simple, it is not straightforward to achieve this goal. There are two major **challenges** that need to be seriously tackled. Firstly, the high-level phase noise in CSI measurements hindered precise control of beamforming direction. Considering that two conditions, *i.e.*, the transceiver pair needs to be synchronized, and the initial value between antenna elements needs to be the same, are not met, the conventional beamforming method can not be directly applied to WiFi sensing systems (radar meets these two conditions because it transmits and receives in one device). Secondly, due to the limited antenna number of existing WiFi devices, it is challenging to form forceful beams to filter out the motion interference from non-target directions. Different from radar systems, since the main lobe generated by limited antennas of commodity WiFi devices may not be strong enough to mitigate the noise from other directions, side lobe interference cannot be ignored in WiFi systems. Furthermore, when the interferers appear in the side lobe direction, the weak respiration signal may be buried in strong motion interference signals.

In this paper, we take the following steps to address the above challenges. Firstly, to enable CSI beamforming with high-noise measurements, we optimize the traditional phase offset calibration schemes by not only eliminating the time-varying phase noise but also addressing the between-antenna phase shift, which may lead to significant deviations in the beam direction [16, 31]. Specifically, we first employ a reference CSI-based algorithm to cancel out the identical hardware noise (*e.g.*, PDD, SFO, CFO) resulting from the asynchronous between WiFi transceivers in time domain [38, 40]. Then, considering that the cycle slips in the phase lock loop (PLL) [7, 16, 51] at each antenna, by using the cross-correlation method, a beam-direction correction (BDC) algorithm is proposed to compensate for the between-antenna phase shift and ensure stable beam generation that accurately aligns the main beam toward the target direction.

Secondly, given the limited antenna number of existing WiFi devices, we explore the noise suppression capability of beam nulls to mitigate the motion interference from interfering directions. In particular, a Directional Nulling BeamForming (DN-BF) algorithm is designed to adaptively suppress the motion interference from other non-target directions via the null scan scheme, as illustrated in Fig. 1. During the beam null scan process, the receiver array sequentially directs the CSI null towards different interference angles while constraining the main lobe to the target direction. Then, by further analyzing the respiration energy of each scanned signal in different directions, we can adaptively find and eliminate the motion interference impacts of interfering angles.

We summarize our contributions as follows:

- We design *Wi-Spatial*, a respiration sensing system that can accurately monitor a target person even in the presence of motion interference. To the best of our knowledge, this is the first system that can monitor respiration accurately amidst motion-interference with one pair of commercial WiFi transceivers.

- By canceling out the identical hardware noises and further compensating the residual initial phase shifts between antennas, stable beamforming schemes are enabled for CSI-based sensing systems, which are proved both theoretically and experimentally.
- By steering the main lobe towards the target person and directing the beam nulls to the interference directions, an anti-motion interference algorithm, DN-BF, is designed to mitigate various intensity motion interference.
- Extensive experiment results based on commodity WiFi show that *Wi-Spatial* outperforms the state-of-the-art (SOTA) systems in various motion interference scenarios and can achieve 0.41 bpm median absolute deviation even in the presence of high-intensity interference[1].

The remainder of this paper is organized as follows: Sec. 2 surveys the related work of human respiration monitoring systems. Then, in Sec. 3, we exploit the feasibility of CSI beamforming and its anti-interference capability. Sec. 4 details the design and implementation of the *Wi-Spatial* system. Next, the experiment settings and the evaluation results of our system are presented in Sec. 5. Finally, we conclude our work in Sec. 7.

2 RELATED WORKS

Numerous studies have been conducted on respiration monitoring. For example, sensors can be either attached to a user's body or placed in proximity to the user to monitor respiration. However, those methods are intrusive[1, 18] or suffer from limited coverage area[22, 49]. Compared with those methods, Radio Frequency (RF)-based approaches provide broader coverage and greater mobility, making them ideal for monitoring in contact-free and ubiquitous scenarios. The design space of these approaches is summarized in Fig. 2.

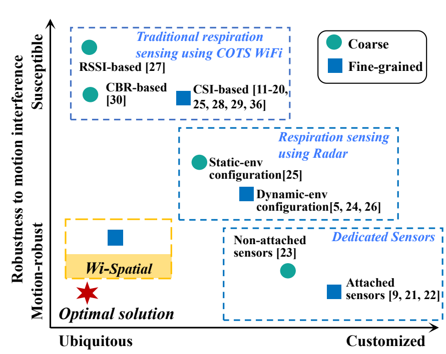

Fig. 2. Design Space: comparing to related work.

Radar-driven approaches. Given the large bandwidth, numerous high-precision respiration sensing systems have been implemented based on radar devices, including frequency-modulated continuous-wave (FMCW) radars[4], ultra-wideband (UWB) pulse radars[48], imaging radars[28], and mmWave radars[25], *etc*. For example, DeMan [28] used an imaging radar to monitor breathing-induced patterns and detect stationary people. V^2iFi [48] utilized the wide 1.4 GHz bandwidth of its IR-UWB radar to discriminate different subjects in a vehicle. By employing two modality data, *i.e.*, mmWave radar and camera data, Var-VSM[25] monitored vital signs for the location-fixed human subject

[1]The high-intensity interference is defined as the motion interference that involves the whole body region of the interferer (*i.e.*, stepping), characterized by its intense movement and a large area of effect.

in the presence of interference from both the motion interference of other people and the body movements of the target individual. Some of these works are capable of achieving satisfactory monitoring robustness even in the presence of motion interference. However, they need dedicated hardware and spectrum, which inevitably adds cost, and lack scalability, which impedes large-scale and long-term deployment.

WiFi-based approaches. WiFi-based respiration sensing approaches have gained particular popularity due to their compatibility with existing communication hardware and widespread deployment. Conventional methods [13, 14, 21, 35, 39] are based on the fact that the wireless channel state shows rhythmic patterns associated with the breathing process of a single person to perform respiration monitoring. For instance, Liu *et al.* [13, 14] presented the first attempt to estimate respiration rate by analyzing the power spectral density (PSD) of CSI amplitude in the frequency domain. Wang *et al.* [21] presented the Fresnel zone model for WiFi-based respiration monitoring. Zeng *et al.* [39] leveraged the complementary CSI amplitude and phase information to improve the system robustness of user location. By utilizing the CSI difference between antennas, the sensing range of WiFi-based respiration monitoring systems was further improved in work[41]. However, these systems are all based on the assumption that there is only one breathing person in the sensing area and thus may not be applicable to real-world scenarios since motion interference from others may occur occasionally.

Recently, some works have been proposed to leverage the physical separation or algorithmic separation methods to realize respiration monitoring under motion interference environments. For example, Hu *et al.*[8] exploited the dominating effect of WiFi near-field and achieved respiration sensing under the interference of other people. Qiu *et al.* [15] enabled respiration monitoring in dynamic environments through the integration of multiple consecutive WiFi channels. However, these approaches required the interferers to keep a sufficient distance from the target person and WiFi transceivers. Zeng *et al.*[40] leveraged the statistical independence of different subjects to separate the respiration signal of each person. However, they fail to identify to whom each respiration signal belongs, thereby introducing potential ambiguity. There also has been a growing interest in leveraging compressed beamforming reports (CBR) for WiFi sensing [27]. Nevertheless, considering that CBR provides only partial and compressed channel information, the coarse-grain data may pose challenges in accurately extracting target signals within complex and dynamic environments.

Summary. Despite extensive research efforts on WiFi-based respiration sensing, there is still an evident gap between research and real-life applications. One of the main reasons for this gap is the underlying assumptions of the ideal environment without any interfering individuals. To address these issues, certain works recommended increasing the resolution of multipath discrimination by increasing bandwidth to achieve anti-motion interference capability [15, 19]. However, these approaches need a wire-direct connection (WDC) to mitigate the accumulating hardware-related noises induced by the process of WiFi channel synthesizing. Recently, researchers have exploited beamforming techniques [38, 43] to reinforce the respiration signals carried by the WiFi dynamic component vector. However, they only focused on the single-person case and totally disregarded common scenarios involving multiple interfering subjects.

3 MOTION NOISE-TOLERABLE CSI BEAMFORMING

In this section, we introduce the basics of WiFi human sensing and systematically study the capability of CSI beamforming for anti-motion interference sensing. Compared with conventional respiration sensing systems developed for human sensing in static environments[40, 41], our system is capable of monitoring the respiration of a target in the presence of motion interference from other persons.

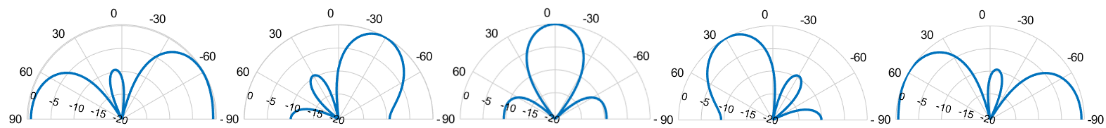

(a) -60° (b) -30° (c) 0° (d) 30° (e) 60°

Fig. 3. Simulation of WiFi Beamforming in different directions (5.32 GHz, 2.8 cm interval, 3-element uniformed linear array).

3.1 WiFi Sensing in Dynamic Environments

The CSI, under an ideal condition, is a complex value to describe the multipath propagation from transmitter to receiver at a certain carrier frequency, which can be represented as:

$$h(f,t) = \sum_{k=1}^{L} \alpha_k(f,t) \cdot e^{-j2\pi \frac{d_k(f,t)}{\lambda}}, \tag{1}$$

where L is the total number of propagation paths, α_k is the amplitude attenuation factor, d_k is length of k^{th} propagation path, and f is the carrier frequency. Consider a WiFi sensing system with a transmitter (Tx) and a receiver (Rx) aiming to sense the physical motion of a human subject $\mathcal{S}$ in a dynamic environment with multiple interferers. To focusing on the influence of the target subject $\mathcal{S}$, we model the CSI between transmitter and receiver as[8]:

$$h(f,t) = h_{T,S,R}(f,t) + h^s_{T,R}(f) + h^d_{T,R}(f,t), \tag{2}$$

where $h_{T,S,R}(f,t)$ represents the channel gain from Tx to Rx through the reflection of the target person $\mathcal{S}$, and $h^s_{T,R}(f)$, $h^d_{T,R}(f,t)$ represent the static and dynamic channel gains between Tx and Rx corresponding to the communication path and interfering motions along it, respectively. Due to the clock unsynchronization between Tx and Rx, the actual CSI readings are mixed with hardware-related noises[15], which can be expressed as:

$$x(f,t) = \alpha_N \cdot e^{-j(k(\lambda_p+\lambda_s)+\lambda_c+\beta)} \cdot h(f,t) + Z, \tag{3}$$

where $x(f,t)$ represents the CSI measurements with hardware-related noises at time t for a specific subcarrier frequency f. Additionally, α_N is the power control gain of the receiver, λ_p, λ_s, and λ_c denote the phase offset of packet detection delay (PDD), sampling frequency offset (SFO), and central frequency offset (CFO), respectively. Furthermore, β represents the initial phase offset, and Z denotes the Gaussian noise. It is worth noting that the initial phase offset β varies from antenna to antenna, which is likely due to the initial phase difference of the phase-locked loop (PLL) or the inherent circuit imperfection in commercial WiFi NICs (*e.g.*, Intel 5300, Intel 9260, Atheros AR9380) [42, 52]. Previous studies have shown that this initial phase offset is semi-time-invariant, usually alternating between two possible values, and similar observations have been reported in the context of angle-of-arrival estimation based on inter-antenna phase [7, 50, 52].

3.2 CSI Beamforming for Directional Sensing

Suppose the WiFi receiver is equipped with a linear antenna array with M elements and that the distance between adjacent antennas is d. Consider a piece of consecutive CSI with a length of L from the antenna array:

$$\begin{aligned} \boldsymbol{X} = [&x_1(1), \cdots, x_1(l), \cdots, x_1(L), \cdots, x_m(1), \cdots, x_m(l), \\ &\cdots, x_m(L), \cdots, x_M(1), \cdots, x_M(l), \cdots, x_M(L)], \end{aligned} \tag{4}$$

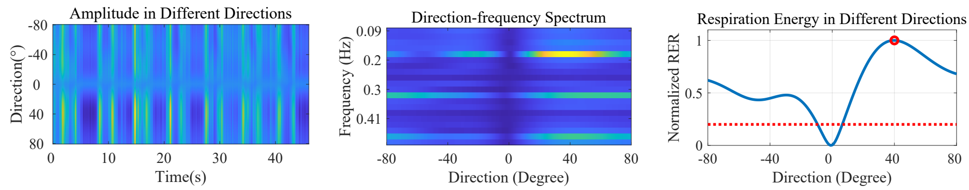

(a) CSI amplitude in different directions before compensation.

(b) The direction-frequency spectrum of beam scanned CSI before compensation.

(c) The RER of beam scanned CSI before compensation.

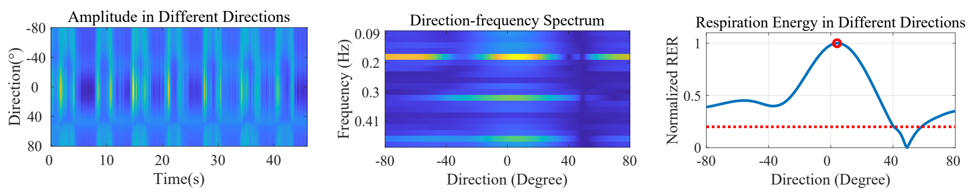

(d) CSI amplitude in different directions after compensation.

(e) The direction-frequency spectrum of beam scanned CSI after compensation.

(f) The RER of beam scanned CSI after compensation.

Fig. 4. One case of respiration energy distribution of beamformed CSI for single person scenario ($\theta = 0°$, $RR = 0.18$ Hz). (a-c) The respiration signal of the subject is strengthened, however, the estimated direction has a large deviation due to the PLL phase offset between antenna elements. (d-f) The beamformed CSI after initial PLL phase offset compensation, however, the energy of side lobes is non-negligible.

where $x_m(l)$ represents the complex CSI value for m_{th} antenna at l_{th} sample. In the multipath probation environment, each propagation path induces a distinct phase shift at each antenna element depending on its incident angle θ. The steering vector $\boldsymbol{a}(\theta)$ corresponding to the incident angle θ can be represented by:

$$\boldsymbol{a}(\theta) = [1, \cdots, e^{j\Delta\varphi_m}, \cdots, e^{j\Delta\varphi_M}]^T, \tag{5}$$

where $\Delta\varphi_m = \frac{2\pi(m-1)dsin(\theta)}{\lambda}$ is the phase delay between the m_{th} and the 1_{st} antenna corresponding to the arrival angle θ. By compensating for the phase shift delay and summing up the signals of antenna elements using $\boldsymbol{a}(\theta)$, the beamformed CSI can be represented as:

$$\boldsymbol{y} = \boldsymbol{a}(\theta)^T \boldsymbol{X}, \tag{6}$$

where $\boldsymbol{y}$ is the beamformed CSI with the main lobe directed to θ. Then, we define a spatial grid of all candidate AoAs $\boldsymbol{A}$ to extract the signals from all azimuth directions. The beamformed CSI of all azimuth directions can be expressed as:

$$\boldsymbol{y} = \boldsymbol{A}^H \boldsymbol{X}, \tag{7}$$

where $\boldsymbol{A}$ is the weight matrix of all candidate AoA values, which could be expressed as:

$$\boldsymbol{A} = \left[\boldsymbol{a}(\theta_1) \quad \boldsymbol{a}(\theta_2) \quad, \cdots, \quad \boldsymbol{a}(\theta_{g_A})\right]^T, \tag{8}$$

where g_A denotes the number of candidate AoA.

Next, we simulate the beam patterns in different directions to test the feasibility of using CSI beamforming for directional respiration sensing. In the simulation, the antenna array is configured with 3 antennas with adjacent intervals of half a wavelength (i.e., 2.8 cm for a frequency of 5.32 GHz). The beam direction is set to −60°, −30°, 0°, 30°, and 60°, respectively. With three-element uniform linear array, the corresponding half-power beamwidth can be approximated as $\Delta\theta_{3dB}$ =

$0.886 \cdot \lambda/(M \cdot \lambda/2) \approx 33.9°$. This beamwidth is narrow enough to direct the main lobe toward the target subject in typical indoor environments. As illustrate in Fig. 3, we can observe that the main lobe is oriented toward the targeted directions and the gain of other directions is much smaller than the main lobe. However, the energy of the side lobes in non-target directions is non-negligible due to the limited number of antenna elements in commodity WiFi devices.

Afterward, we carry out a benchmark experiment to validate the capability of main lobe generation for a three-antenna array, as illustrated in Fig. 4. In the experiment, a target person is positioned in front of the receiving antenna array ($\theta = 0°$), and his respiration rate (RR) of 0.18 Hz that measured by a commodity ECG sensor node[2]. We then apply the approach presented in [43] to generate the directions-frequency spectrum for spectral analysis. The results clearly demonstrate that after beamforming, a sharp and stable spectral peak emerges precisely at 0.18 Hz. This indicates that the three-antenna array can enhance the target's respiratory signal. In other words, the main lobe can be directed toward the target user. According to [43], for one person, the direction-frequency spectrum is expected to show one bright spot in the direction corresponding to the target person. However, **the target direction does not exhibit the highest respiratory energy, instead, it demonstrates the lowest intensity of the respiratory energy.** One of the main reasons behind this is the initial phase offset of actual CSI readings across different receiver antennas, which will be addressed in Sect. 3.4.

3.3 Directional Nulling Beamforming for Motion-tolerance Sensing

To address the issue of side lobe interference, we propose a Directional Nulling Beamforming (DN-BF) method, which directs the main lobe to the target direction while adaptively nulling the motion interference signals from interferers in other directions.

In theory, a linear antenna array with M elements can control the main lobe direction while controlling up to $M-1$ null directions [20]. With three antennas of commercial WiFi transceivers, the array can generate a main beam while placing nulls in up to two distinct directions. Conventional beamformers that leverage beam nulls to suppress the interfering noise (e.g., Minimum Variance Distortionless Response, MVDR), formulate as an optimizing problem. By minimizing the total output power while constraining the gain of the target direction, the interference from other directions can be suppressed[25]. The problem is formulated as follows:

$$\begin{gathered} \min_{\boldsymbol{w}} \boldsymbol{w}^H \boldsymbol{R} \boldsymbol{w} \\ s.t. \boldsymbol{w}^H \boldsymbol{a}(\theta) = 1, \end{gathered} \tag{9}$$

where $\boldsymbol{R}, \boldsymbol{w}$ represent the covariance matrix of the received signals and the complex weight applied to the beamformer, respectively. Whereas the optimized MVDR beamformer can theoretically achieve a higher signal-to-noise ratio (SNR), they were not designed to prioritize sensing quality.

Therefore, we need to find another "ruler" to measure the sensing quality of human respiration. We adopt the sensing-signal-to-noise-ratio (SSNR) defined in [38] to quantify the human sensing quality. In typical monitoring scenarios, the direction or position of the target user is usually fixed, while those of non-target individuals are typically random, *e.g.*, in a hospital ward with multiple patients. Therefore, let us assume the directions of motion interferers are unknown, while the target user's direction is known. The problem of motion-tolerance CSI beamforming is formulated as follows:

$$\begin{gathered} \max_{\boldsymbol{w}} ssnr \\ s.t. \boldsymbol{w}^H \boldsymbol{a}(\theta_{\mathcal{S}}) = 1, \end{gathered} \tag{10}$$

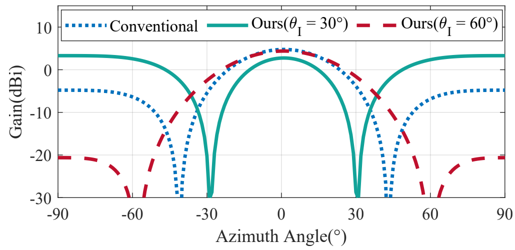

Fig. 5. Comparison of beam patterns between conventional beamforming and DN-BF. With the main lobe direction determined (i.e., $\theta_{\mathcal{S}} = 0°$), the null position of the conventional beamformer is fixed, whereas DN-BF allows for placing beam nulls at a specific direction (e.g., $\theta_I = 30°, \theta_I = 60°$).

where *ssnr* is defined as the ratio of the power of dynamic component and noise:

$$ssnr = \frac{P_{target}}{P_{noise}} = \frac{|\alpha_{\mathcal{S}}(f,t)|^2}{|\epsilon(f,t)|^2}, \tag{11}$$

where P_{target} denotes the power of the target-reflected signal, P_{noise} denotes the noise power, $\alpha_{\mathcal{S}}(f,t)$ represents the amplitude attenuation of the signal reflected from the target subject, and $\epsilon(f,t)$ represents the measurement noise on subcarrier f at time t. As we can observe from Eq. (11), a higher target-reflected signal power or a lower noise power results in a larger SSNR, and thus indicates a stronger sensing capability.

Since the SSNR defined in Eq. (11) has not yet taken into account the noise components caused by motion interference in dynamic environments, we extend the SSNR to be suitable for measuring sensing quality in motion interference environments and define it as follows:

$$ssnr = \frac{P_{target}}{P_{interferer} + P_{noise}} = \frac{|\alpha_{\mathcal{S}}(f,t)|^2}{|\alpha_I(f,t)|^2 + |\epsilon(f,t)|^2}, \tag{12}$$

where $P_{interferer}$ denotes the power of motion interference, and $\alpha_I(f,t)$ represents the amplitude attenuation of the signal reflected from the motion interferers.

Assuming that the target subject is at angle $\theta_{\mathcal{S}}$ and the interferer is at angle θ_I, the SSNR of the beamformed signal can be represented as:

$$ssnr = \frac{|\boldsymbol{w}^H \boldsymbol{a}(\theta_{\mathcal{S}})\boldsymbol{x}(f,t)|^2}{|\boldsymbol{w}^H \boldsymbol{a}(\theta_I)\boldsymbol{x}(f,t)|^2 + |\epsilon(f,t)|^2}, \tag{13}$$

where $\boldsymbol{a}(\theta_{(\cdot)})\boldsymbol{x}(f,t)$ is the signal of direction $\theta_{(\cdot)}$. Thus, the problem is formulated as follows:

$$\max_{\boldsymbol{w}} \frac{|\boldsymbol{w}^H \boldsymbol{a}(\theta_{\mathcal{S}})\boldsymbol{x}(f,t)|^2}{|\boldsymbol{w}^H \boldsymbol{a}(\theta_I)\boldsymbol{x}(f,t)|^2 + |\epsilon(f,t)|^2} \tag{14}$$

$$s.t. \boldsymbol{w}^H \boldsymbol{a}(\theta_{\mathcal{S}}) = 1. \tag{15}$$

By substituting the constraints $\boldsymbol{w}^H \boldsymbol{a}(\theta_{\mathcal{S}}) = 1$ into the objective function, the optimization problem can be reformulated as follows:

$$\max_{\boldsymbol{w}} \frac{1}{|\boldsymbol{w}^H \boldsymbol{a}(\theta_I)|^2 + \sigma^2}, \tag{16}$$

$$\text{s.t. } \boldsymbol{w}^H \boldsymbol{a}(\theta_{\mathcal{S}}) = 1, \tag{17}$$

where $\sigma^2 = \frac{|\epsilon(f,t)|^2}{|\boldsymbol{x}(f,t)|^2}$ denotes the noise-to-signal ratio. Since σ^2 can be assumed approximately constant over a short time window [26], it does not affect the optimization structure. By converting

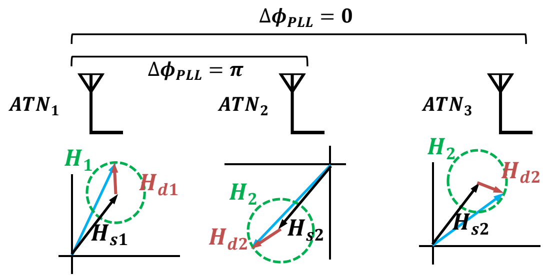

Fig. 6. Illustration of between-antenna π-shift phase offset.

the maximum optimization problem to a minimum optimization problem and simplifying the formula, we can obtain:

$$\min_{\boldsymbol{w}} \frac{\left|w^H(a(\theta_I))\right|^2 + \sigma^2}{\left|w^H a(\theta_S)\right|^2} \tag{18}$$

$$s.t.\boldsymbol{w}^H \boldsymbol{a}(\theta_S) = 1, \tag{19}$$

where $|\boldsymbol{w}^H \boldsymbol{a}(\theta_I)|^2$ represents the power gain of the direction of the interferer, $\boldsymbol{w}^H \boldsymbol{a}(\theta_S)$ represents the gain of target direction, and σ^2 is the noise term. The minimum interference can be achieved by minimizing the signal power of the interfering direction while constraining the target gain.

Fig. 5 illustrates the comparison between the conventional phase-shift beamformer and DN-BF. These results demonstrate that DN-BF has a strong capability of placing beam nulls in a specified direction while maintaining the direction of the main lobe. Therefore, when an interferer is present in random unknown directions with the predefined target direction, DN-BF can adaptively mitigate motion interference using the beam null scan scheme. Specifically, during the beam null scan process, DN-BF constrains the main lobe to the direction of the target person while sequentially placing beam nulls towards different azimuth angles. By analyzing the respiration energy (RER) of each scanned signal, we can select the target respiration signal with the lowest motion interference.

3.4 Enable Stable CSI Beamforming via Initial Phase Offset Compensations

As explained in Sec. 3.1, the beamforming technology cannot be directly employed for WiFi-based respiration sensing due to the hardware-related noise of CSI measurements. To realize DN-BF on off-the-shelf WiFi devices, we leverage two steps to enable stable CSI Beamforming via phase compensations: (1) time-varying phase noise removal, which cancels out the identical hardware noise between antennas (*e.g.*, PDD, SFO, CFO), and (2) between-antenna phase shift calibration, which compensates the phase offset among receiver antenna.

Time-varying phase offset removing for CSI Beamforming. By adding a reference channel, the obtained CSI ratio can subdue time-varying hardware-related noises[23, 24, 41]. We utilize an optimization-based approach to construct the reference CSI without requiring any additional hardware. The reference CSI is represented as follows:

$$h_{ref} = W^H X \tag{20}$$

where $W = \begin{bmatrix} r_1 e^{j\epsilon_1} & r_2 e^{j\epsilon_2} & \cdots & r_M e^{j\epsilon_M} \end{bmatrix}$ is a $1 \times M$ weight vector with $2M$ parameters. The weighted vector W can be obtained by minimizing the energy of dynamic frequency components, which can be expressed as:

$$W = \arg\min_{W} re(W^H X) \tag{21}$$

where $re(\cdot)$ is the energy of the dynamic frequency component, which can be calculated by taking the Fast Fourier Transform (FFT) over a time window to CSI phase information. Note that instead of minimizing the respiration energy ratio (RER) of CSI amplitude as in [38], we directly minimize the energy of human motions of CSI phase information to construct the reference CSI. This is mainly because the calculated RER is a relatively small value and using it as the optimization function may result in residual dynamic components in the constructed reference CSI. The weighted sum of signals is given by:

$$\begin{aligned}\sum_{i=1}^{M} W_i \cdot x_i(f,t) &= \sum_{i=1}^{M} W_i \cdot e^{-j(\phi_T+(\beta_0+\Delta\beta_i))} \cdot [h^S_{T,R}(f) + h^D_{T,R}(f,t)] \\ &= e^{-j\phi_T} \sum_{i=1}^{M} W_i \cdot [h^S_{T,R}(f) + h^D_{T,R}(f,t)] \cdot e^{-j(\beta_0+\Delta\beta_i)} \\ &= e^{-j\phi_T} \sum_{i=1}^{M} [W_i \cdot h^S_{T,R}(f) + W_i \cdot h^D_{T,R}(f,t)] \cdot e^{-j(\beta_0+\Delta\beta_i)},\end{aligned} \tag{22}$$

where $\phi_T = k(\lambda_p + \lambda_s) + \lambda_c$ represents the random time-varying phase offsets induced by PDD, SFO, and CFO that is equivalent to CSI for each receiver antenna, $e^{-j\Delta\beta_i} = e^{-j(\beta_i-\beta_0)}$ represents the initial phase offsets of i_{th} antenna with respect to the 1^{st} antenna $e^{-j\beta_0}$, and $h^D_{T,R}(f,t) = h_{T,S,R}(f,t) + h^d_{T,R}(f,t)$ represents the overall dynamic components of CSI which contain both the signal of the target person and the interference signal of interferers. After minimizing the human motion energy of CSI in the frequency domain, the optimal weight W^* can be obtained. The constructed reference CSI can be expressed as:

$$h_{ref}(f,t) = e^{-j\phi_T} \sum_{i=1}^{M} W^*_i \cdot h^S_{T,R}(f) \cdot e^{-j\beta_i} = e^{-j\phi_T} b, \tag{23}$$

where $b = \sum_{i=1}^{M} W^*_i \cdot h^S_{T,R}(f) \cdot e^{-j(\beta_0+\Delta\beta_i)}$ is a complex-valued constant. By calculating the ratio between the CSI of each antenna and the reference CSI, we can subdue the hardware-related time-varying phase noises. The denoised CSI of the i_{th} antenna can be calculated as:

$$\frac{x_i(f,t)}{h_{ref}(t)} = (\widehat{h^S_{T,R}(f)} + \widehat{\alpha^D_{T,R}} e^{\frac{-j2\pi d_i(f,t)}{\lambda}}) \cdot e^{-j(\beta_0+\Delta\beta_i)}, \tag{24}$$

where $\widehat{h^S_{T,R}} = h^S_{T,R}/b$ is the constant static component and $\widehat{\alpha^D_{T,R}} e^{\frac{-j2\pi d_i(t)}{\lambda}}$ is the calibrated dynamic component. Now, the random time-varying phase noise has been eliminated. However, the between-antenna chains phase noise $e^{-j\Delta\beta_i}$ still exists.

Between-antenna phase offset removing for CSI Beamforming. After removing the time-varying phase offset, there is still an initial constant phase offset between the antenna pairs of the receiver, as illustrated in Fig. 6. To understand its impact on CSI beamforming, we consider a simple beamforming process using two RF chains. Let $h_0(f,t)$ and $h_1(f,t)$ denote the CSI of two RF chains, with θ denoting the angle of arrival of the signal reflected by the target individual. We have the beamformed CSI of combined RF chains as follows:

$$y(\theta,t) = h_0(f,t) + h_1(f,t) \cdot e^{j\frac{2\pi sin(\theta)}{\lambda}}. \tag{25}$$

Considering the initial random between-antenna phase offset, we have:

$$\begin{aligned}y(\theta,t) &= e^{-j\beta_0} h_0(f,t) + e^{-j\beta_1} h_1(f,t) \cdot e^{j\frac{2\pi sin(\theta)}{\lambda}} \\ &= e^{-j\beta_0} [h_0(f,t) + h_1(f,t) \cdot e^{j\frac{2\pi sin(\theta)}{\lambda}} \cdot e^{j(\beta_1-\beta_0)}],\end{aligned} \tag{26}$$

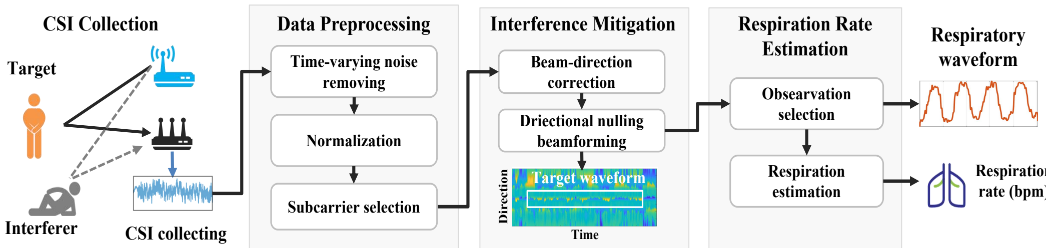

Fig. 7. The system pipeline of *Wi-Spatial*.

where $e^{j(\beta_1-\beta_0)}$ represents the between-antenna phase offset and can potentially disrupt the direction of the CSI beam. Fortunately, the phase difference between two antennas has two constant values, and the relationship between those two values is given by [7]:

$$|\beta_1 - \beta_0| = k\pi, \quad k \in 0, 1, 2, \dots, N \tag{27}$$

where β_0 and β_1 represent the initial phase of the 1^{st} and 2^{ed} antenna at the same receiver, respectively. This phenomenon is called π-shift [7], which may be due to the imperfection of the inertial circuits or the initial phase difference of the phase-locked loop (PLL) of commercial off-the-shelf (COTS) WiFi chips [7, 52]. Therefore, we can compensate for the π-shift between antennas to correct the CSI beam pattern. Our method is presented in Algo. 1, and we will discuss it in detail in the next section.

As shown in Fig. 4 (d-f), it can be observed that before the initial phase shift compensation, the direction of the generated beam has a significant deviation. After compensating the π-shift offset, the beam direction of CSI has been aligned with the corresponding steering vector $\boldsymbol{a}(\theta)$, which indicates that the denoised CSI can be applied to beamforming methods. Note that there are slight deviations between the direction of the maximum respiratory energy and the ground truth direction. This is mainly because we have assumed that the target direction is the angle of the subject relative to the Rx antenna array, while the actual incidence angle needs to take into account the signal propagation process from the transmitter to the subject and then to the receiver. Additionally, we can also observe that the relatively high-energy respiration signals appear in the directions of the side lobes (*e.g.*, +60° and -60°), which indicates that the interference from the side lobes is non-negligible. For instance, when the interferer appears in the direction of a side lobe, the signal we extract will contain not only the respiratory signal amplified by the main lobe but also the interference signal amplified by the side lobe.

4 SYSTEM DESIGN

4.1 System Overview

Fig. 7 illustrates the pipeline of our system. The goal of our design is to achieve motion interference-tolerance respiration sensing. *Wi-Spatial* is mainly composed of three components: : data preposessing, interference mitigation, and respiration rate estimation. The data preprocessing module first eliminates the time-varying phase offsets from raw CSI measurements, then denoises and normalizes the data. Then, the most sensitive subcarrier is selected to mitigate the impact of frequency selective fading. Subsequently, the interference mitigation module performs the PLL phase offset compensation algorithm to eliminate the phase offset between antennas and correct the CSI beam direction. After that, the DN-BF is employed to mitigate the motion interference signal from non-target persons. Finally, the respiration rate estimation module extracts the CSI phase waveform with the lowest motion interference and estimates the respiration rate of the target person.

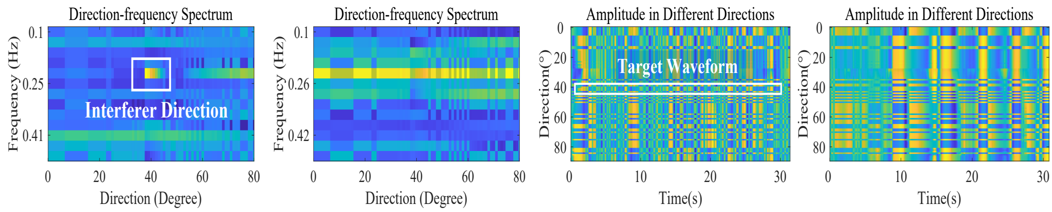

(a) Low SSNR ($\theta_I = 45°$). (b) High SSNR (no interferer). (c) Low SSNR ($\theta_I = 45°$). (d) High SSNR (no interferer).

Fig. 8. Examples of DN-BF with different levels of SSNR. (a),(c) the CSI amplitude and direction-frequency spectrum after the DN-BF scan under a high SSNR (i.e., no interference) scenario. (b), (d) the case under low SSNR (e.g., high interference).

4.2 Data Preprocessing

Commodity WiFi NIC reports noisy CSI values, both due to the unsynchronized clock between transceiver devices and the low resolution of the analog-to-digital converters (ADCs). Therefore, to enable CSI beamforming on commercial WiFi devices, we have the following three preprocessing steps: 1) address the time-varying phase offset, 2) normalize the magnitude of complex-valued CSI, and 3) select the sensitive subcarrier.

Time-varying phase offsets removing. For each subcarrier, we cancel out the time-varying phase offsets through two steps as described in Sec. 3.4. First, to construct the reference CSI, we take the FFT to the phase of the combined CSI over a time window of 20 seconds and calculate the energy of human motion by the energy sum of FFT bins in the range of 0.1-10 Hz[2]. The optimal weight W^* is obtained by minimizing the human motion energy by a genetic algorithm [5]. Second, once the optimal weight W^* is obtained, we constructed the reference CSI based on Eq.(20), where $h_{ref} = W^{*H}X$, and divided it to each antenna to eliminate the time-varying phase offsets.

CSI Denoising and Normalization. After removing time-varying phase offsets, the CSI time series is filtered and normalized so that the samples across different antennas can be identical in CSI amplitude to facilitate subsequent beamforming and accurate respiration waveform recovery. We first identify the outliers using the three-sigma statistical threshold criteria method and replace these outliers using linear interpolation. Then, we denoised the CSI through a low-pass filter with a cut-off frequency of $f_{cut} = 0.5$ Hz for respiration monitoring. Afterward, we subtracted the direct current (DC) components of CSI for static background elimination and scaled the magnitude for CSI dynamic components normalization. This allows us to focus on the phase change of dynamic components.

Subcarrier Selection. The sensitivity of capturing the target subject's respiration signals varies among different subcarriers due to the multipath fading and shadowing effects at different frequencies. Therefore, we just select the high-quality observations for anti-motion interference respiration sensing. We adopt the method proposed in [40] to select the most sensitive subcarrier. Based on the phenomenon that a higher RER of a time series of CSI readings for a certain subcarrier indicates a higher possibility that it contains useful respiration information, the sensitive subcarrier can be selected.

4.3 Motion-interference Mitigation

Beam direction correction (BDC). According to Sec. 3.4, the between-antenna phase shift $e^{j(\beta_j - \beta_i)}$ may induce a large deviation in the beam direction. Thus, before applying DN-BF to

[2]The normal range for human respiration rate is 0.1-0.5 Hz, while human activity frequencies range from 0-10 Hz.

suppress the motion-induced interference from other individuals, we first compensate for the phase shift between antennas. The initial PLL phase offsets of a certain antenna element are two possible constant values[7, 42], and the phase difference between two antennas remains two possible values for one frequency channel as described in Eq. (27).

The pseudo-code of the PLL phase offset compensation is shown in Algo. 1. The input of the algorithm is the time-varying phase offset calibrated CSI sequence, which is denoted as $H = (\hat{h_1}, \hat{h_2}, \cdots, \hat{h_M})$. The phase compensation is based on the following insight. When the phase offset in each RF chain is correctly compensated, the CSI values between the 2^{nd} to M^{th} antenna and the 1^{st} antenna exhibit the highest similarity. It should be noted that once the PLL phase offset values are determined, they are long-term valid unless the Rx devices are restarted. After compensating the PLL phase offset, we can obtain the denoised CSI, which is taken as the input of CSI DN-BF to mitigate the motion interference from other persons.

DN-BF based motion interference suppression. We direct the main lobe to the target direction while scanning the directions ranging from $-80°$ to $80°$ with beam nulls (at a step size of $1°$). However, due to the lack of precise knowledge about $\epsilon(f, t)$, directly obtaining a nontrivial solution by solving Eq. (18) is infeasible. To address this, we employ an optimization algorithm to determine the optimal DN-BF weights. For computational efficiency, we reformulate the optimization function as follows:

$$\boldsymbol{w}^* = \arg\min_{\boldsymbol{w}} c_1 \boldsymbol{w}^H \boldsymbol{a}(\theta_I) - c_2 \boldsymbol{w}^H \boldsymbol{a}(\theta_T) \tag{28}$$

where c_1 and c_2 are scale factors that ensure the main lobe is steered toward θ_T. Specifically, we set the c_1 to about approximately ten times c_2 to maintain this constraint. Once the $\boldsymbol{w}^*$ is obtained, we multiplied the denoised CSI signal by the corresponding weight of DN-BF for each direction. This process generates a set of beam patterns, each of which enhances the reflected signals from the target direction while suppressing motion noise from the corresponding interference direction using beam nulls.

Algorithm 1: PLL Phase Offset Compensation

Input: Time-varying phase offsets calibrated CSI of M RF chains: $H = (h_1, h_2, \cdots, h_M)$,
reference CSI, h_{ref}
Output: Compensated CSI data, $H' = (h'_1, h'_2, \cdots, h'_M)$,
values of phase offset $\hat{\varphi}$

Initialize the PLL phase offset compensation set,
$\phi \leftarrow \{0, \pi\}$;
for *i = 2 to M* **do**
    similarity = **Null**;
    for *j = 1 to length(ϕ)* **do**
        Calibrate h_i using ϕ_j, $h_{tmp} \leftarrow h_i + \phi_j$;
        similarity[j] $\leftarrow \sum_{i=1}^{n}(||h_{tmp\,i} - h_{1i}||)/(L-1)$;
    end
    Ind $\leftarrow$ index of min(similarity);
    values of phase offset $\hat{\varphi}_i \leftarrow \phi_{Ind}$;
    $h'_i \leftarrow$ compensating h_i with $\hat{\varphi}_i$;
end
return $H', \hat{\varphi}$;

4.4 Respiration-induced Path Identification and Respiration Rate Estimation

Observation selection. After obtaining the DN-BF processed beamformed CSI for each direction, we calculate the unwrapped CSI phase information as candidate waveforms. Afterward, we generate

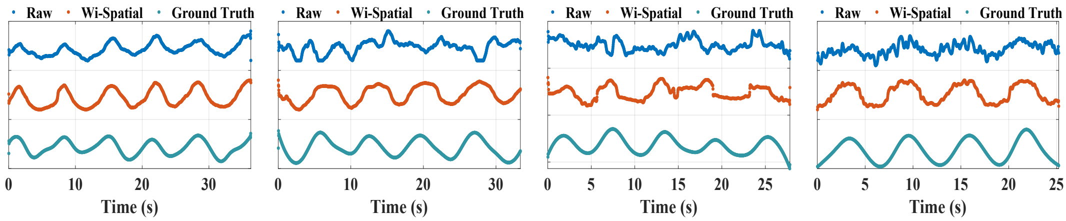

(a) No interference. (b) Low interference (breath). (c) Medium interference (hand-wave). (d) High interference (step).

Fig. 9. Examples of respiration waveform recovery from three types of interference action.

the direction-frequency spectrogram for interference analysis. Firstly, we denoise the candidate waveforms using a band-path filter in the range of human respiration rate (0.1-0.5 Hz). Then, we apply the FFT to each candidate waveform to generate the direction-frequency spectrogram, which characterizes the distribution of respiration energy in various directions. For each candidate waveform, the SSNR is calculated as the ratio between the sum of the bins corresponding to the respiratory frequency range (*i.e.*, 0.1-0.5 Hz) and the sum of the bins corresponding to the noise energy. The noise energy is estimated as the residual energy (*i.e.*, the total energy minus the respiration signal energy).

Fig. 8 illustrates two DN-BF examples with different levels of SSNR, where both of them have a target direction of 0° relative to the receiver antenna array. The example with higher SSNR was collected in a static environment without any interferer, while the example with lower SSNR was collected with an interferer performing a stepping action at a direction of 45°. From the generated direction-frequency spectrogram in Fig. 8 (a)(c), one can observe that the respiration energy levels across all directions exhibit a consistently high magnitude. This is because the main lobe of DN-BF is always directed toward the target. Consequently, in the absence of interfering motion or when the interference is weak, mitigating signals from other directions does not effectively enhance the respiration energy in the target direction. Conversely, in the low-SSNR case, steering the beam null toward the interferer effectively mitigates interference, leading to a significant improvement in the target's RER. Therefore, based on this observation, we select candidate waveforms from the direction with the strongest respiratory energy for respiration sensing.

Respiration estimation. Once the respiration waveform is extracted, we employ the autocorrelation function (ACF) [44] to estimate the respiration rate. Based on the calculated ACF, the periodic breath cycle can be measured by the horizontal distance between the origin and the peak. We utilize ACF for respiration rate estimation since it can shorten the time delay and produce instantaneous estimation.

5 EVALUATION

In this section, we evaluate *Wi-Spatial*'s performance in estimating respiration rates under both static and motion interference conditions. We examine various scenarios and parameter settings to assess the system's accuracy.

5.1 Experiment Methodology

Implementation. As shown in Fig. 11, *Wi-Spatial* consists of one transmitter and receiver pair. All transceivers are off-the-shelf mini-PCs equipped with an Intel 5300 wireless NIC. Devices are set to work in the monitor mode on channel 64 at 5.32 GHz with a 20 MHz bandwidth to avoid radio interference [11]. The transmitter activates one antenna and broadcasts WiFi packets at a rate of

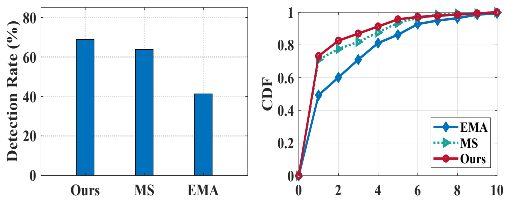

(a) Detection rate. (b) Estimation Error.

Fig. 10. Overall Performance.

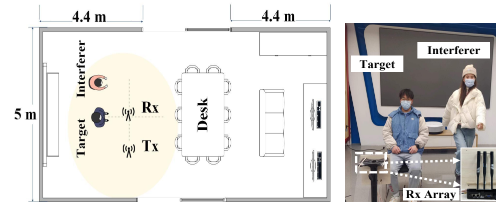

Fig. 11. Experimental setup.

1,000 packets per second. The receiver activates all three antennas, with the antenna spacing set to half the wavelength of the WiFi signal. We collect the ground-truth respiration waveform with a shimmer ECG sensor node[2] attached to the participant's chest. The CSI tool [6] is utilized for the CSI collection, and we process the CSI data offline using MATLAB on a DELL Vostro 5890 desktop computer.

Evaluation setup. To fully explore the performance of *Wi-Spatial*, we conduct extensive experiments on respiration rate estimation in both static and dynamic environments where the target person and non-target participants are spatially separated. We place the antennas of Tx and Rx at a distance of 1.5 m apart, with the target person being monitored in front of the Rx. All the transceivers are held up at a height of 10 dm, corresponding to the ergonomic sitting and breathing level of users. The *Wi-Spatial* is deployed in a home-like environment. We recruited 9 healthy volunteers (5 males and 4 females) of different heights (185 to 160 cm) and weights (50 to 79 kg) to participate in experiments. The ages of volunteers vary from 18 to 25.

We collect respiration data in the presence of non-target persons performing various types of interfering behaviors (*e.g.*, breath, handwave, and step), representing different levels of interference (*e.g.*, low, medium, and high). These levels correspond to the size of the body region affected by the movement interference, with low-level interference involving small localized movements, medium-level interference affecting the upper body region, and high-level interference impacting the entire body. During data collection, the participants were asked to work in groups of four, with one person acting as the target and one to three others acting as dynamic interferers. The target person is asked to sit (quasi-)statically, while the interferer is asked to perform different interference behaviors in different positions, directions, and distances. Note that the distance between the interferer and the receiver is always equal to or greater than the distance between the target subject and the receiver to recreate daily breathing monitoring scenarios under non-intentional motion interference.

Baseline. We compare our technique with two WiFi-based respiration monitoring systems in terms of respiration rate accuracy under dynamic backgrounds with motion interference - an independent component analysis (ICA)-based multi-person signal separation method named MultiSense (MS) in [40] and a beamforming-based method named EMA [38]. Note that since the MS cannot identify to whom each respiration pattern belongs based on the ICA algorithm, we select the waveform whose estimation is closer to the ground truth for comparison.

Metrics. We use two metrics: 1) Median Absolute Deviation (MAD), defined as the median of absolute error compared with the ground truth in each slipping window during one measurement; and 2) Detection rate [41], defined as $\frac{N_{dt}}{N}$, where the N_{dt} is the number of CSI measurements whose respiration rate estimation is close to the ground truth (absolute error < 0.5 bpm) and N is the total number of collected CSI samples.

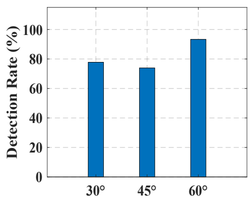

(a) Separation angle.

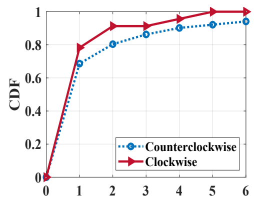

(b) Rotation.

Fig. 12. Impact of different separation angles.

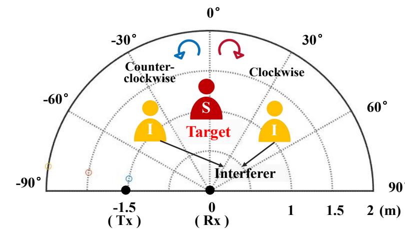

Fig. 13. Experimental setup with different separation angles.

5.2 Overall Performance and Comparison

As illustrated in Fig. 9, we first present four examples of respiration waveform recovery by *Wi-Spatial* under different intensity levels of motion interference. For motion interference, we divide it into four levels: static, low, medium, and high. We represent these levels with four interference behaviors: no interference, breathing interference, handwaving interference, and stepping interference. To ensure a clear comparison, the examples presented are all from the same target subject, with only one interferer in the environment. The waveforms illustrated from top to bottom represent the raw CSI signal, recovered respiration waveform, and ground truth waveform. It is evident that *Wi-Spatial* captures the respiration waveform of the target subject accurately, even in environments with high motion interference. Moreover, in low and medium interference scenarios, *Wi-Spatial* captures not only the accurate respiration rate but also the respiration pattern of the target person.

Table 1. Comparison of overall estimation errors.

	Overall	Static Environment	Dynamic Environment		
			Breath	Hand wave	Step
EMA	1.01	0.18	0.84	1.67	0.9
MS	0.36	0.2	0.29	0.51	0.42
Ours	**0.28**	**0.19**	**0.27**	**0.42**	**0.41**

We further report the quantitative evaluation results and compare them with baselines by applying the metrics defined earlier. As shown in Tab. 1, it can be seen that when the sensing environments are static (*i.e.*, no interferer in the sensing area), all the systems work well, with *Wi-Spatial* achieving a comparable high level of accuracy (*i.e.*, 0.19 bpm). However, when motion interference occurs, *Wi-Spatial* outperforms the other two systems. Note that while MS achieves accuracy comparable to *Wi-Spatial*, it does not address the challenge of matching the extracted signal to the corresponding target. In our replication, we selected the waveform that best corresponded to the target, which likely led to an overestimation of MS's accuracy under motion interference.

As shown in Fig. 10(a) and Fig. 10(b), it can be seen that *Wi-Spatial* achieves the highest detection rate of 68.8%, while the same quality for MS and EMA is 63.7% and 41.3%, respectively. For MAD of all samples, *Wi-Spatial* achieves an overall median error of 0.28 bpm, while the baseline method has the overall median errors of 0.36 bpm and 1.01 bpm. In summary, all the results demonstrate *Wi-Spatial*'s ability to achieve anti-motion interference respiration sensing in dynamic backgrounds.

5.3 System Robustness to Interference Factors

In the following, we study the performance of *Wi-Spatial* under different motion interference scenarios.

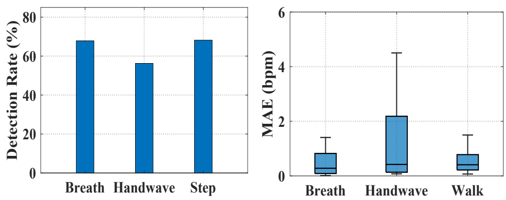

(a) Detection rate. (b) Estimation Error.

Fig. 14. Impact of motion-interference type.

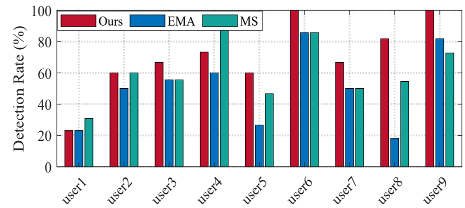

Fig. 15. Impact of different subjects.

5.3.1 Impact of separation angle. We first conduct a two-subject experiment to evaluate the impact of the separation angle between the target person and the interfering person. The separation angle is a key factor in *Wi-Spatial*'s motion interference mitigation ability that directly affects the performance of the system. A separation angle smaller than the beam width may cause the target signal to be inseparable from the interference signal, while a larger separation angle might be susceptible to side lobes. In this experiment, both the interferer and target person are put 1.5 m away from the receiver. We put the target person at 0° and the interferer at 30°, 45°, and 60°, respectively. To maintain other factors constant, we instructed both the target person and the interferer to engage in natural breathing.

The results are shown in Fig. 12(a). The system errors decrease as the separation angle increases. When the subjects get closer, the interference nulling ability of DN-BF declines, and the two subjects' reflected signals are superimposed. The reason behind this is that when the direction of nulls is small enough, the main lobe width of DN-BF will not continue to shrink to ensure that the gain in the target direction is high enough.

As illustrated in Fig. 13, we further investigate the impact of the rotation direction of interferers on our system. In this experiment, the interferer is put at the same separation angle but in a different rotation direction, where the angles are measured clockwise as positive and counterclockwise as negative. We vary the separation angle while keeping other factors unchanged (*i.e.*, −45° and 45°). The angle +45° corresponds to the direction away from the Tx-Rx axis, with the Rx is set as the origin in the polar coordinate system.

The statistical results are shown in Fig. 12(b). The MAD under these settings is 0.38 bpm and 0.16 bpm for the counterclockwise and clockwise directions, respectively. Comparing the two experimental settings, the interferer is in the clockwise direction, which will result in a comparatively weaker interference. This is because of the physical separation of the WiFi device transceiver. When the interferer is located away from the transmitter, the reflected signal caused by the interference will exhibit a smaller magnitude, thereby leading to diminished interference to the system.

5.3.2 Impact of Subject Diversity. The main challenge of monitoring the respiration of a target person under motion interference is that reflections from a strong target may overwhelm the reflections from a weak target [34]. Various factors, such as body shape, movement patterns, and other variables, can exert different impacts on motion interference across different subjects. Thus, we evaluate the impact of subject diversity across all 9 volunteers, encompassing variations in height, weight, and gender. For each scenario, we repeat the experiment with those three different interfering motions.

The performance of *Wi-Spatial* for all 9 subjects is presented in Fig. 15, showing a detection rate greater than 60% for 8 subjects and for the rest still have a median error lower than 2 bpm. This is because the respiration signals of different individuals exhibit inherent variations, particularly

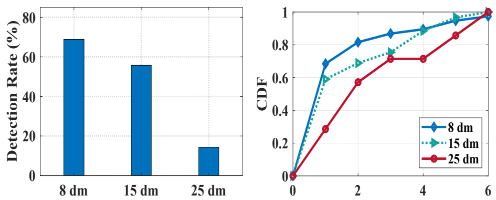

(a) Detection rate. (b) MAD.

Fig. 16. Impact of distance between device and target subject.

(a) Breath. (b) Hand wave. (c) Step.

Fig. 17. Experimental setup with different types (intensities) of motion interference.

among individuals with weaker breathing movements, which can be easily buried by interference from other individuals. Compared with baseline, *Wi-Spatial* demonstrates robust performance in motion interference scenarios, even when the interferers exhibit diverse characteristics. Although the performance of *Wi-Spatial* is lower than that of MultiScense in the data from user 1 and user 4, it achieves good performance in most cases. Note that MultiScense is unable to distinguish which extracted waveform corresponds to the target. Therefore, in our experiments, we selected the waveform that most closely resembled the target signal for comparison. This selection process may have resulted in an overestimation of MultiScense's accuracy.

5.3.3 Impact of the Type (Intensity) of Interfering Motion. In real-world scenarios, *Wi-Spatial* should be capable of handling situations where the interferer performs various types of motion with different intensities. Therefore, we investigate the performance of *Wi-Spatial* under varying levels of motion interference intensity. The levels of motion interference intensity are defined based on the extent of the body area involved in motion, where larger movement regions correspond to higher interference intensity. For example, breathing involves minimal movement confined to the chest area, resulting in low interference, whereas hand waving engages the upper body, causing moderate interference, and stepping utilizes the entire body, leading to high interference. We conduct two-target sensing tests, with the subject sitting in front of the receiver as the monitoring target. We vary the motion intensity from low to high while keeping other factors unchanged. As illustrated in Fig. 17, the levels of interfering intensity ranged from low to high, represented by breathing, hand waving, and stepping, respectively.

As shown in Fig. 14, *Wi-Spatial* achieves a median error lower than 0.5 bpm for all types of interference motion. However, it might be counter-intuitive that the accuracy of medium interference (hand waving interference) is comparatively lower when compared to high interference (stepping interference). This might be attributed to the similarity between CSI variations induced by hand waving and those induced by breathing, yet the magnitude of CSI variation induced by hand waving is larger.

5.3.4 Impact of the number of interferers. In real-life scenarios, the presence of multiple interferers is frequently observed. To study the impact of the number of interferers, we vary the number of non-target subjects from 0 to 3, as illustrated in Fig. 19. The target position was set at 0°, while the interferers were distributed in directions equal to or greater than 36.38° to avoid the cluster merge when the separation angle is smaller than the Rx half-power beamwidth (36.38°). The target is positioned at a distance of 0.8 m from the receiver, while the interferer's position is intentionally set beyond 1.5 m to prevent crowding.

The results are shown in Fig. 18 (a). The system errors increase when the number of interferers increases. When the number of interferers reaches three, the error of *Wi-Spatial* increases significantly. This can be attributed to the selective suppression mechanism of DN-BF, which positions the

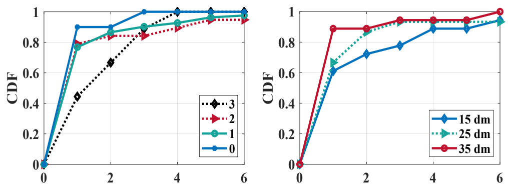

(a) Number of interferers. (b) Distance of interferers.

Fig. 18. Impact of interferer number and distance.

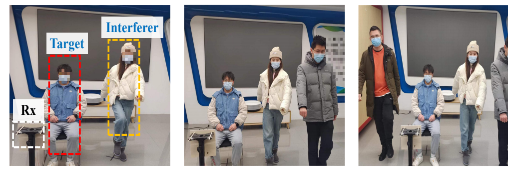

(a) One interferer. (b) Two interferers. (c) Three interferers.

Fig. 19. Experimental setup with the different number of interferers.

beam null in the direction of the strongest motion interference. However, since the beam reshaping is optimized for a single null position, its effectiveness in mitigating interference diminishes when multiple interferers are present.

5.3.5 Impact of the distance between WiFi devices and the target subject. The distance between the Rx antenna array and the target subject can affect the sensing performance. To evaluate the impact of the distance between the WiFi devices and the target subject, we conduct a two-subject experiment. We let the target subject vary their distance from 0.8 m to 2.5 m and keep other factors unchanged (*i.e.*, 30° and 1.5 m away from the receiver). We repeat the experiments for each interfering motion.

As shown in Fig. 16, as the distance increases, the detection rate declines from 68.8% at 0.8 m to 14.3% at 2.5 m. This performance reduction is primarily attributed to inaccurate initial phase-offset calibration caused by the weakened CSI strength at longer distances. Although beamforming theoretically enhances long-range sensing by amplifying signals in the target direction, its performance is constrained by the imperfections of the commodity linear antenna array. As the strength of the target-reflected signal decreases substantially, the accuracy of phase-offset calibration diminishes, which in turn leads to beam misalignment and degraded DN-BF performance.

5.3.6 Impact of the distance between interferer and Rx. The distance between the interferer and Rx can also affect the sensing performance. Therefore, we conduct a two-subject experiment to evaluate the impact of the distance between the interfering person and the receiver. We let the interferer vary their distance from 1.5 m to 3.5 m and keep their direction unchanged (*i.e.*, 30°). We repeat the experiments for each interfering motion. The target person's position is set at 0° and 0.8 m away from the receiver.

The results are shown in Fig. 18 (b). The system errors increase when the distance between the interferer and receiver decreases. When the interferer moves closer, the motion interference becomes stronger, making it more challenging to decompose the target and interference signals. However, even at the nearest distance of 1.5 m, *Wi-Spatial* can still achieve a median error of 0.45 bpm, which is enough for most applications, thus firmly proving the effectiveness of our system.

5.4 Effectiveness of the Components of *Wi-Spatial*

In the following, we demonstrate the efficacy of employing our proposed methods for anti-motion interference respiration sensing.

5.4.1 Effectiveness of BDC. The beam-direction corrector (BDC) compensates for the initial phase offset among antenna elements. It is a crucial preprocessing step for enabling beamforming-based perception on commercial WiFi devices. This step is especially important when precise and controllable beam patterns are required.

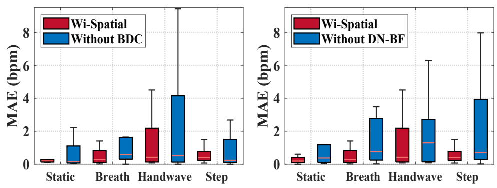

(a) BDC.

(b) DN-BF.

Fig. 20. Effectiveness of the Components of *Wi-Spatial*.

	Overall	Static Environment	Dynamic Environment		
			Breath	Handwave	Step
-DN-BF	0.72	0.37	0.75	1.29	0.71
-BDC	0.35	0.17	0.59	0.51	0.23
All	**0.28**	**0.19**	**0.27**	**0.42**	**0.41**

Table 2. Effectiveness of the components of *Wi-Spatial*.

To assess the impact of BDC on reducing motion interference in respiration monitoring, we evaluate the performance of *Wi-Spatial* both with and without it. Without the BDC, the direction of the beam may experience significant deviation, resulting in the main lobe being misaligned with the target. This misalignment leads to inadequate signal enhancement in the intended direction, potentially compromising the system's accuracy. For the experiments without BDC, we used the same experimental configuration as in Sec. 5.1, except that we omitted the PLL phase offset compensation before applying DN-BF.

The results are shown in Fig. 20 (a) and Tab. 2. The absolute errors without the BDC for these three types of motion interference are 0.59 bpm, 0.51 bpm, and 0.23 bpm, respectively. In comparison, respiration monitoring with the BDC yields errors of 0.27 bpm, 0.42 bpm, and 0.41 bpm. This demonstrates a significant decline in system performance under motion-interference conditions without the BDC. Therefore, it is evident that the BDC module enhances the controllability of beam pattern generation, thereby improving overall system reliability.

5.4.2 Effectiveness of DN-BF. The DN-BF is the key module to suppress the motion-interference signal from other directions. It adaptively positions the beam null to the interfering directions to mitigate the motion interference.

To evaluate the efficacy of the DN-BF algorithm, we validate the performance of *Wi-Spatial* both with and without it. In the absence of DN-BF, the acquired CSI data consists of three denoised streams. To ensure a fair comparison, we select the data stream with the highest RER. This ensures that any observed improvement in accuracy results from DN-BF's suppression of motion noise, rather than simply a low inherent level of motion noise in the collected CSI data.

The results are shown in Fig. 20 (b) and Tab. 2. The MAD without the DN-BF for these three types of motion interference are 0.75 bpm, 1.29 bpm, and 0.71 bpm, respectively. In contrast, with DN-BF enabled, the errors are reduced to 0.27 bpm, 0.42 bpm, and 0.41 bpm. This significant performance decline in motion-interference scenarios highlights the effectiveness of DN-BF in mitigating motion noise.

In summary, all these results have demonstrated the effectiveness of the BDC and DN-BF for respiration rate estimation in motion-interference scenarios.

6 LIMITATION AND DISCUSSION

6.1 Predetermined Sensing Area

Due to the high energy of side lobes when applying conventional beamforming to WiFi CSI, we present the directional nulling beamforming (DN-BF) method to suppress the motion interference from other directions. While our method significantly reduces the motion interference from non-target individuals, it assumes prior knowledge of the target's direction. The reason behind this is that when the motion interference from non-target individuals has similar frequency characteristics with the target user, the identity of each signal source becomes ambiguous. For instance, if both the target and the interferers are performing breathing motions simultaneously, relying solely on the spectral properties is inadequate to identify the target's breathing signal. One potential solution is to incorporate new features that can distinguish signals from the target user and the interferer, such as distance information [8] and motion pattern [15, 32].

6.2 Requirement of Sufficient Separation

When we perform respiration signal extraction using the DN-BF method, a sufficient separation angle between the interferer and the target person is necessary for proper distinction. Empirically, this separation angle should be greater than 35°, which is close to the half-power beam width of WiFi beamforming. However, it is not always possible to meet this requirement in real-life environments. For instance, there may be multiple subjects in close spatial proximity in a sleeping scene. Basically, there are two ways to address the challenging issue. One is to adopt more advanced WiFi protocols, such as 802.11ac, which support more antennas and wider frequency bandwidth. For instance, the 802.11ac standard theoretically allows up to 8 antennas per NIC card, enabling a stronger main lobe and improved control over beamforming nulls. The other solution is to employ the multi-source separation method to separate the signals of multiple individuals, e.g., the WiFi-based system MultiSense[40].

6.3 Applicability for Multi-Target Sensing

The current system is primarily designed for anti-motion interference respiration sensing in single-target scenarios. We believe that this is an important use case, particularly for hospital ward scenarios, which aims to ensure the accurate monitoring of a single in-place patient even when other individuals are present, such as the attending nurses or nearby patients. Nevertheless, simultaneous monitoring of multiple targets' respiration is also an important direction for optimizing our system, as monitoring multiple targets can enhance both the functionality and applicability. A feasible way to extend the proposed DN-BF method to multi-target sensing is to first perform beam scanning to estimate the angular positions of multiple users. Once these directions are identified, DN-BF can then be applied individually to each direction to enhance the corresponding target signal while suppressing interference from other users. It should be noted that the effectiveness of this approach depends on the angular separation among users and the number of antennas available. With sufficient angular separation and antenna resources, this extension is practical.

7 CONCLUSION

This paper presents *Wi-Spatial*, a WiFi-based sensing system that supports respiration monitoring in motion-interference scenarios. Different from prior work, *Wi-Spatial* exploits the multi-objective beamforming to suppress noise from interfering directions. As the CSI measurements of the commodity WiFi antenna array are buried with between-antenna phase noise, we design the beam direction correction method to address the challenge of generating controllable CSI beam patterns. Additionally, since the high energy of side lobes may amplify the signal from noisy directions when applying conventional beamforming to WiFi sensing systems, we propose a novel directional nulling beamforming (DN-BF) method to adaptively suppress the motion interference of non-target interferers. Extensive experiments show that *Wi-Spatial* can achieve accurate respiration monitoring with a median absolute respiration deviation of 0.41 bpm even in the presence of intensity stepping interference with only a pair of WiFi transceivers. In future works, more fascinating applications can be implemented on the proposed anti-motion interference respiration sensing.

8 ACKNOWLEDGEMENTS

This work is supported by Major Scientific and Technological Project of Anhui Provincial Science and Technology Innovation Platform (Grant No. 202305a12020012), National Natural Science Foundation of China (Grant No. 62302145, No. 62422213, No. U23A20303, No. 62372149, and No. 62572168), Beijing Nova Program (20240484641), the Anhui Provincial Natural Science Foundation (Grant No. 2508085MF151), Fundamental Research Funds for the Central Universities (Grant No. JZ2025HGTB0225), Key Laboratory of Space-Air-Ground Integrated Network Security, Ministry of Industry and Information Technology, and Shandong Key Laboratory of Advanced Computing.

REFERENCES

[1] Khizar Anjum and Dario Pompili. 2024. Battery-less Implantable Continuous EEG Monitoring via Anisotropic Diffusion. *IEEE Journal on Selected Areas in Communications* (2024).

[2] Adrian Burns, Barry R Greene, Michael J McGrath, Terrance J O'Shea, Benjamin Kuris, Steven M Ayer, Florin Stroiescu, and Victor Cionca. 2010. SHIMMER™–A wireless sensor platform for noninvasive biomedical research. *IEEE Sensors Journal* 10, 9 (2010), 1527–1534.

[3] Lili Chen, Kai Chen, Jie Xiong, Ke Li, Sunghoon Ivan Lee, Fuwei Wang, Zhanyong Tang, Zheng Wang, Dingyi Fang, and Xiaojiang Chen. 2022. Toward wide-area contactless wireless sensing. *IEEE/ACM Transactions on Networking* 31, 2 (2022), 590–605.

[4] Yonathan Eder and Yonina C Eldar. 2023. Sparsity-Based Multi-Person Non-Contact Vital Signs Monitoring Via FMCW Radar. *IEEE journal of biomedical and health informatics* (2023).

[5] Zhengxin Guo, Wenyang Yuan, Linqing Gui, Biyun Sheng, and Fu Xiao. 2023. BreatheBand: A fine-grained and robust respiration monitor system using WiFi signals. *ACM Transactions on Sensor Networks* 19, 4 (2023), 1–18.

[6] Daniel Halperin, Wenjun Hu, Anmol Sheth, and David Wetherall. 2011. Tool release: Gathering 802.11 n traces with channel state information. *ACM SIGCOMM computer communication review* 41, 1 (2011), 53–53.

[7] Feiyu Han, Chengchen Wan, Panlong Yang, Hao Zhang, Yubo Yan, and Xiang Cui. 2020. ACE: Accurate and automatic CSI error calibration for wireless localization system. In *2020 6th International Conference on Big Data Computing and Communications (BIGCOM)*. IEEE, 15–23.

[8] Jingzhi Hu, Tianyue Zheng, Zhe Chen, Hongbo Wang, and Jun Luo. 2023. MUSE-Fi: Contactless muti-person sensing exploiting near-field Wi-Fi channel variation. In *Proceedings of the 29th Annual International Conference on Mobile Computing and Networking*. 1–15.

[9] Jinyang Huang, Jia-Xuan Bai, Xiang Zhang, Zhi Liu, Yuanhao Feng, Jianchun Liu, Xiao Sun, Mianxiong Dong, and Meng Li. 2024. Keystrokesniffer: An off-the-shelf smartphone can eavesdrop on your privacy from anywhere. *IEEE Transactions on Information Forensics and Security* (2024).

[10] Jinyang Huang, Yuanhao Feng, Feng-Qi Cui, Xiang Zhang, Zhi Liu, Xin Liu, Jianchun Liu, Fusang Zhang, and Meng Li. 2026. Identifying Who You Are No Matter What You Write through Abstracting Handwriting Style. *IEEE Transactions on Dependable and Secure Computing* (2026), 1–15. https://doi.org/10.1109/TDSC.2026.3668275

[11] Jinyang Huang, Bin Liu, Chenglin Miao, Xiang Zhang, Jiancun Liu, Lu Su, Zhi Liu, and Yu Gu. 2023. Phyfinatt: An undetectable attack framework against phy layer fingerprint-based wifi authentication. *IEEE Transactions on Mobile Computing* (2023).

[12] Siheng Li, Beihong Jin, Zhi Wang, Fusang Zhang, Xiaoyong Ren, and Haiqin Liu. 2024. Leveraging Attention-reinforced UWB Signals to Monitor Respiration during Sleep. *ACM Transactions on Sensor Networks* 20, 5 (2024), 1–28.

[13] Jian Liu, Yan Wang, Yingying Chen, Jie Yang, Xu Chen, and Jerry Cheng. 2015. Tracking vital signs during sleep leveraging off-the-shelf wifi. In *Proceedings of the 16th ACM international symposium on mobile ad hoc networking and computing*. 267–276.

[14] Liu, Xuefeng and Cao, Jiannong and Tang, Shaojie and Wen, Jiaqi. 2014. Wi-sleep: Contactless sleep monitoring via wifi signals. In *2014 IEEE Real-Time Systems Symposium*. IEEE, 346–355.

[15] Jiefan Qiu, Pan Zheng, Kaikai Chi, Ruiji Xu, and Jiajia Liu. 2022. Respiration Monitoring in High-Dynamic Environments via Combining Multiple WiFi Channels Based on Wire Direct Connection Between RX/TX. *IEEE Internet of Things Journal* 10, 2 (2022), 1558–1573.

[16] Vishnu V Ratnam, Bilal Sadiq, Hao Chen, Wei Sun, Shunyao Wu, Boon Loong Ng, and Jianzhong Zhang. 2024. WiDRa: Enabling Millimeter-Level Differential Ranging Accuracy in Wi-Fi Using Carrier Phase. *IEEE Journal on Selected Areas in Communications* 42, 9 (2024), 2410–2423.

[17] Masaaki Sakuraya, Eri Douno, Wakana Iwata, Akihiro Takaba, Kosuke Hadama, Natsuki Kawamura, Toshinori Maezawa, Kei Iwamoto, Yuya Yoshino, and Kenichi Yoshida. 2022. Accuracy evaluation of mainstream and sidestream end-tidal carbon dioxide monitoring during noninvasive ventilation: a randomized crossover trial (MASCAT-NIV trial). *Journal*

of Intensive Care 10, 1 (2022), 1–9.
[18] Osman Salem, Khalid Alsubhi, Ahmed Mehaoua, and Raouf Boutaba. 2020. Markov models for anomaly detection in wireless body area networks for secure health monitoring. *IEEE Journal on Selected Areas in Communications* 39, 2 (2020), 526–540.
[19] Shuyu Shi, Yaxiong Xie, Mo Li, Alex X Liu, and Jun Zhao. 2019. Synthesizing wider WiFi bandwidth for respiration rate monitoring in dynamic environments. In *IEEE INFOCOM 2019-IEEE Conference on Computer Communications*. IEEE, 181–189.
[20] Harry L Van Trees. 2002. *Optimum array processing: Part IV of detection, estimation, and modulation theory.* John Wiley & Sons.
[21] Hao Wang, Daqing Zhang, Junyi Ma, Yasha Wang, Yuxiang Wang, Dan Wu, Tao Gu, and Bing Xie. 2016. Human respiration detection with commodity WiFi devices: Do user location and body orientation matter?. In *Proceedings of the 2016 ACM international joint conference on pervasive and ubiquitous computing*. 25–36.
[22] Meng Wang, Jinyang Huang, Xiang Zhang, Zhi Liu, Meng Li, Peng Zhao, Huan Yan, Xiao Sun, and Mianxiong Dong. 2024. Target-oriented wifi sensing for respiratory healthcare: from indiscriminate perception to in-area sensing. *IEEE Network* (2024).
[23] Xuyu Wang, Chao Yang, and Shiwen Mao. 2017. TensorBeat: Tensor decomposition for monitoring multiperson breathing beats with commodity WiFi. *ACM Transactions on Intelligent Systems and Technology (TIST)* 9, 1 (2017), 1–27.
[24] Xuyu Wang, Chao Yang, and Shiwen Mao. 2020. On CSI-based vital sign monitoring using commodity WiFi. *ACM Transactions on Computing for Healthcare* 1, 3 (2020), 1–27.
[25] Yingqi Wang, Zhongqin Wang, J Andrew Zhang, Haimin Zhang, and Min Xu. 2023. Vital Sign Monitoring in Dynamic Environment via mmWave Radar and Camera Fusion. *IEEE Transactions on Mobile Computing* (2023).
[26] Zhongqin Wang, J Andrew Zhang, Min Xu, and Y Jay Guo. 2022. Single-target real-time passive WiFi tracking. *IEEE Transactions on Mobile Computing* 22, 6 (2022), 3724–3742.
[27] Chenhao Wu, Xuan Huang, Jun Huang, and Guoliang Xing. 2023. Enabling ubiquitous wifi sensing with beamforming reports. In *Proceedings of the ACM SIGCOMM 2023 Conference*. 20–32.
[28] Chenshu Wu, Zheng Yang, Zimu Zhou, Xuefeng Liu, Yunhao Liu, and Jiannong Cao. 2015. Non-invasive detection of moving and stationary human with WiFi. *IEEE Journal on Selected Areas in Communications* 33, 11 (2015), 2329–2342.
[29] Yue Wu, Fan Li, Yadong Xie, Yu Wang, and Zheng Yang. 2023. SymListener: detecting respiratory symptoms via acoustic sensing in driving environments. *ACM transactions on sensor networks* 19, 1 (2023), 1–21.
[30] Yingxiao Wu, Haocheng Ni, Changlin Mao, Jianping Han, and Wenyao Xu. 2023. Non-intrusive human vital sign detection using mmwave sensing technologies: A review. *ACM Transactions on Sensor Networks* 20, 1 (2023), 1–36.
[31] Yalong Xiao, Junfeng Zhu, Shigeng Zhang, Xuan Liu, and Song Guo. 2023. Fall-attention: An attention-based fall detection method for adjoint activities. *IEEE Transactions on Mobile Computing* 23, 7 (2023), 7895–7909.
[32] Xuecheng Xie, Dongheng Zhang, Yadong Li, Yang Hu, Qibin Sun, and Yan Chen. 2024. Robust WiFi Respiration Sensing in the Presence of Interfering Individual. *IEEE Transactions on Mobile Computing* (2024).
[33] Chao Yang, Xuyu Wang, and Shiwen Mao. 2020. Respiration monitoring with RFID in driving environments. *IEEE Journal on Selected Areas in Communications* 39, 2 (2020), 500–512.
[34] Qian Yang, Hengxin Wu, Qianyi Huang, Jin Zhang, Hao Chen, Weichao Li, Xiaofeng Tao, and Qian Zhang. 2023. Side-lobe can know more: Towards simultaneous communication and sensing for mmWave. *Proceedings of the ACM on Interactive, Mobile, Wearable and Ubiquitous Technologies* 6, 4 (2023), 1–34.
[35] Hüseyin Yiğitler, Ossi Kaltiokallio, Roland Hostettler, Alemayehu Solomon Abrar, Riku Jäntti, Neal Patwari, and Simo Särkkä. 2019. RSS models for respiration rate monitoring. *IEEE Transactions on Mobile Computing* 19, 3 (2019), 680–696.
[36] Gu Yu, Meng Wang, Peng Zhao, Yantong Wang, Hao Zhou, Yusheng Ji, and Celimuge Wu. 2022. Spirofi: Contactless pulmonary function monitoring using wifi signal. In *2022 IEEE/ACM 30th International Symposium on Quality of Service (IWQoS)*. IEEE, 1–10.
[37] Songcan Yu, Qinglin Yang, Junbo Wang, and Celimuge Wu. 2024. Fedusl: A federated annotation method for driving fatigue detection based on multimodal sensing data. *ACM Transactions on Sensor Networks* (2024).
[38] Youwei Zeng, Jinyi Liu, Jie Xiong, Zhaopeng Liu, Dan Wu, and Daqing Zhang. 2021. Exploring multiple antennas for long-range WiFi sensing. *Proceedings of the ACM on Interactive, Mobile, Wearable and Ubiquitous Technologies* 5, 4 (2021), 1–30.
[39] Youwei Zeng, Dan Wu, Ruiyang Gao, Tao Gu, and Daqing Zhang. 2018. FullBreathe: Full human respiration detection exploiting complementarity of CSI phase and amplitude of WiFi signals. *Proceedings of the ACM on Interactive, Mobile, Wearable and Ubiquitous Technologies* 2, 3 (2018), 1–19.
[40] Youwei Zeng, Dan Wu, Jie Xiong, Jinyi Liu, Zhaopeng Liu, and Daqing Zhang. 2020. MultiSense: Enabling multi-person respiration sensing with commodity wifi. *Proceedings of the ACM on Interactive, Mobile, Wearable and Ubiquitous Technologies* 4, 3 (2020), 1–29.

[41] Youwei Zeng, Dan Wu, Jie Xiong, Enze Yi, Ruiyang Gao, and Daqing Zhang. 2019. FarSense: Pushing the range limit of WiFi-based respiration sensing with CSI ratio of two antennas. *Proceedings of the ACM on Interactive, Mobile, Wearable and Ubiquitous Technologies* 3, 3 (2019), 1–26.

[42] Dongheng Zhang, Yang Hu, Yan Chen, and Bing Zeng. 2019. Calibrating phase offsets for commodity wifi. *IEEE Systems Journal* 14, 1 (2019), 661–664.

[43] Fusang Zhang, Zhaoxin Chang, Jie Xiong, Rong Zheng, Junqi Ma, Kai Niu, Beihong Jin, and Daqing Zhang. 2021. Unlocking the beamforming potential of LoRa for long-range multi-target respiration sensing. *Proceedings of the ACM on Interactive, Mobile, Wearable and Ubiquitous Technologies* 5, 2 (2021), 1–25.

[44] Feng Zhang, Chenshu Wu, Beibei Wang, Min Wu, Daniel Bugos, Hangfang Zhang, and K. J. Ray Liu. 2021. SMARS: Sleep Monitoring via Ambient Radio Signals. *IEEE Transactions on Mobile Computing* 20, 1 (2021), 217–231. https://doi.org/10.1109/TMC.2019.2939791

[45] Xiang Zhang, Yu Gu, Huan Yan, Yantong Wang, Mianxiong Dong, Kaoru Ota, Fuji Ren, and Yusheng Ji. 2023. Wital: A cots wifi devices based vital signs monitoring system using nlos sensing model. *IEEE Transactions on Human-Machine Systems* (2023).

[46] Youwei Zhang, Feiyu Han, Panlong Yang, Yuanhao Feng, Yubo Yan, and Ran Guan. 2024. Wi-Cyclops: Room-scale WiFi sensing system for respiration detection based on single-antenna. *ACM Transactions on Sensor Networks* 20, 4 (2024), 1–24.

[47] Peng Zhao, Jinyang Huang, Xiang Zhang, Zhi Liu, Huan Yan, Meng Wang, Guohang Zhuang, Yutong Guo, Xiao Sun, and Meng Li. 2024. Wi-pulmo: Commodity wifi can capture your pulmonary function without mouth clinging. *IEEE Internet of Things Journal* (2024).

[48] Tianyue Zheng, Zhe Chen, Chao Cai, Jun Luo, and Xu Zhang. 2020. V2iFi: In-vehicle vital sign monitoring via compact RF sensing. *Proceedings of the ACM on Interactive, Mobile, Wearable and Ubiquitous Technologies* 4, 2 (2020), 1–27.

[49] Xiaolong Zheng, Kun Yang, Jie Xiong, Liang Liu, and Huadong Ma. 2024. Pushing the limits of WiFi sensing with low transmission rates. *IEEE Transactions on Mobile Computing* (2024).

[50] Xiaokang Zhou, Wei Liang, I Kevin, Kai Wang, Katsutoshi Yada, Laurence T Yang, Jianhua Ma, and Qun Jin. 2025. Decentralized federated graph learning with lightweight zero trust architecture for next-generation networking security. *IEEE Journal on Selected Areas in Communications* (2025).

[51] Yiwei Zhuo, Hongzi Zhu, Hua Xue, and Shan Chang. 2017. Perceiving accurate CSI phases with commodity WiFi devices. In *IEEE INFOCOM 2017-IEEE Conference on Computer Communications*. IEEE, 1–9.

[52] Anatolij Zubow, Piotr Gawłowicz, and Falko Dressler. 2021. On phase offsets of 802.11 ac commodity WiFi. In *2021 16th Annual Conference on Wireless On-demand Network Systems and Services Conference (WONS)*. IEEE, 1–4.